

# **Y-doped $\text{LiZr}_2(\text{PO}_4)_3$ in PVDF-HFP Composite Electrolyte for Solid State Li Metal Batteries**

Pratiksha Gami<sup>a</sup>, Manish Badole<sup>a</sup>, Hari Narayanan Vasavan<sup>a</sup>, Asish Kumar Das<sup>a</sup>, Samriddhi  
Saxena<sup>a</sup>, and Sunil Kumar<sup>a,b,\*</sup>

<sup>a</sup>Department of Metallurgical Engineering and Materials Science, Indian Institute of Technology  
Indore, Simrol, 453552, India.

<sup>b</sup>Center for Electric Vehicle and Intelligent Transport Systems, Indian Institute of Technology  
Indore, Simrol, 453552, India

\* Corresponding author

Corresponding author E-mail: [sunil@iiti.ac.in](mailto:sunil@iiti.ac.in)

## Abstract

Due to their improved electrochemical behavior, ceramic/polymer solid composite electrolytes (CE) are the front runners for application in all-solid-state lithium cells. In this work, a NASICON-type  $\text{Li}_{1.2}\text{Y}_{0.2}\text{Zr}_{1.8}(\text{PO}_4)_3$  (Y-LZP) ceramic powder was prepared using the solid-state synthesis route. Rietveld refinement of XRD data showed that Y-LZP exhibited a single rhombohedral phase ( $R\bar{3}c$  space group) and a grain conductivity  $\sim 5.31 \times 10^{-5} \text{ S cm}^{-1}$  at room temperature. Further, Y-LZP ceramic powder was incorporated in PVDF-HFP/LiTFSI polymer electrolyte to fabricate free-standing, flexible CE membranes of thickness  $\sim 60 \mu\text{m}$ . The CE with 15% inorganic filler (CE15) showed the highest conductivity of  $\sim 5.78 \times 10^{-5} \text{ S cm}^{-1}$  at room temperature with an activation energy of  $\sim 0.43 \text{ eV}$ . A galvanostatic lithium plating-stripping test was performed on the symmetric  $\text{Li}|\text{CE15}|\text{Li}$  cell at a current density of  $0.1 \text{ mA cm}^{-2}$ , and the sample demonstrated lithium plating-stripping stability over 400 h. Linear sweep voltammetry measurements on the symmetric cell confirmed the electrochemical stability of the composite electrolyte to be up to  $\sim 4.67 \text{ V}$ . The electrochemical behavior of an all-solid-state cell fabricated using  $\text{LiMn}_2\text{O}_4$  cathode and CE15 electrolyte is also reported.

**Keywords:** Electrochemistry; Composite electrolytes; NASICON; Ionic conductivity; Transference number; All-solid-state lithium cells.

## 1. Introduction

Uninterrupted, efficient, and reliable energy sources are vital for modern society. Renewable energy sources are important to maintain the freedom of mobility and for global decarbonization. As a power source, batteries are becoming a crucial component of sustainable transportation. The rechargeable Li-ion batteries have been effective for a wide array of energy storage applications ranging from small portable consumer electronics to electric vehicles due to their excellent energy density, long cycle life, high voltage, no memory effect, wide electrochemical window, stable charge-discharge process, among the other benefits.<sup>1-3</sup>

However, liquid electrolytes pose serious safety hazards (like thermal runaway and explosion due to mechanical/thermal/electric abuse) in Li-ion batteries.<sup>4-6</sup> In contrast, solid electrolytes reduce such safety issues in lithium metal batteries.<sup>7</sup> Moreover, the mechanical strength of solid electrolytes could suppress the formation of lithium dendrites, allowing the use of the high specific capacity lithium metal as the anode in all-solid-state batteries.<sup>8-11</sup> Solid electrolytes are broadly classified into three categories based on their composition: solid inorganic electrolytes (SIEs), solid polymer electrolytes (SPEs), and solid composite electrolytes (SCEs). NASICON (Na Super Ionic CONductor) type inorganic materials are one of the most promising candidates for the application as Li-ion conducting solid electrolytes due to their decent ionic conductivity ( $> 10^{-5}$  S  $\text{cm}^{-1}$ ) and wide electrochemical stability window ( $\sim 5$  V).<sup>12, 13</sup> Hong and Goodenough reported the first NASICON-type compositions with the general formula  $\text{Na}_{1+x}\text{Zr}_2\text{Si}_x\text{P}_{3-x}\text{O}_{12}$  ( $0 \leq x \leq 3$ ).<sup>14, 15</sup> Since then, numerous lithium analog NASICON-type  $\text{LiM}_2(\text{PO}_4)_3$  with  $M = \text{Zr}, \text{Ti}, \text{Ge}, \text{Sn}$ , etc. compositions have been synthesized with various aliovalent/isovalent substitutions to improve the bottleneck area for Li-ion migration, increase Li-ion concentration, and suppress the secondary

phase formation.<sup>13, 16-20</sup> Depending on compositions and sintering conditions, NASICON-type  $\text{LiZr}_2(\text{PO}_4)_3$  (LZP) displays a complex polymorphism with different structures (*Triclinic*, *Monoclinic*, *Rhombohedral*, *Orthorhombic*). Among these, rhombohedral LZP shows the highest room temperature (RT) Li-ion conductivity ( $\sim 10^{-5} \text{ S cm}^{-1}$ ). It has been reported that the substitution of  $\text{Y}^{+3}$  at the Zr-site in LZP stabilizes the rhombohedral in  $\text{Li}_{1.15}\text{Y}_{0.15}\text{Zr}_{1.85}(\text{PO}_4)_3$  phase with a total Li-ion conductivity of  $\sim 3.5 \times 10^{-5} \text{ S cm}^{-1}$ .<sup>21</sup> Although ceramic electrolytes have certain advantages (electrochemical stability,  $\text{Li}^+$  conductivity, mechanical strength), their brittle nature, high electrolyte-electrode interfacial resistance, and high processing costs limit their commercial applications.<sup>22</sup>

SPEs are a combination of polymers, e.g., Polyethylene oxide (PEO), Polyvinylidene fluoride (PVDF), Polyvinyl alcohol (PVA), Polyvinylidene fluoride-co-hexafluoropropylene (PVDF-HFP), Polymethyl methacrylate (PMMA), Polyvinyl pyrrolidone (PVP), etc. and different Li-salts ( $\text{LiTFSI}$ ,  $\text{LiFSI}$ ,  $\text{LiClO}_4$ ).<sup>23, 24</sup> SPEs generally exhibit flexibility and good interfacial contact with electrodes and can accommodate the volumetric expansion of electrodes during the charge-discharge cycle. Still, poor mechanical strength and low RT ionic conductivity have limited the commercialization of SPEs to a large extent.<sup>25-29</sup> Copolymerization, cross-linking, in-situ copolymerization, blending, etc., are being investigated to improve these properties.<sup>27, 30, 31</sup> Ceramic-polymer composite electrolytes can improve ionic conductivity and better mechanical strength.<sup>32-39</sup> Numerous investigations have demonstrated that surface groups such as Lewis acid sites of ceramic fillers can link with Lewis base sites of alkali-ion in the polymer matrix, which promotes the polymer matrix to release more alkali-ions and subsequently increase the ionic conductivity.<sup>40, 41</sup>

In this work, rhombohedral  $\text{Li}_{1.2}\text{Y}_{0.2}\text{Zr}_{1.8}(\text{PO}_4)_3$  was produced by the solid-state reaction route and exhibited a grain conductivity of  $5.31 \times 10^{-5} \text{ S cm}^{-1}$  at RT. Further, the Y-LZP powder was used as the filler in Lithium bis(trifluoromethylsulfonyl)imide (LiTFSI) lithium salt + polyvinylidene fluoride-co-hexafluoropropylene (PVDF-HFP) polymer matrix for the fabrication of free-standing *ceramic-in-polymer* type composite electrolyte (CE) membranes. The CE's lithium-ion conductivity is improved by the extra lithium-ion transport channels through the Y-LZP ceramic particles. The electrochemical behavior of the prepared CE15 electrolyte membrane with Li metal as an anode and  $\text{LiMn}_2\text{O}_4$  as a cathode in an all-solid-state lithium metal cell is also reported.

## 2. Experimental

### 2.1 Material Synthesis

Polycrystalline powder of  $\text{Li}_{1.2}\text{Y}_{0.2}\text{Zr}_{1.8}(\text{PO}_4)_3$  (Y-LZP) was synthesized *via* a solid-state reaction method. Stoichiometric amounts of  $\text{Li}_2\text{CO}_3$ ,  $\text{Y}_2\text{O}_3$ ,  $\text{ZrOCl}_2 \cdot 8\text{H}_2\text{O}$ , and  $\text{NH}_4\text{H}_2\text{PO}_4$  were mixed with an agate mortar and pestle, followed by a planetary ball mill in EtOH for 12 h. 5% extra  $\text{Li}_2\text{CO}_3$  was added to compensate lithium loss. After ball-milling, the ceramic slurry was dried overnight at 80 °C in a drying cabinet to remove EtOH. The dried powder was then heated at 600 °C for 12 h. Afterward, the powder was ground in a planetary ball mill for 6 h and dried overnight. Subsequently, the powders were uniaxially pressed under 200 MPa to fabricate cylindrical pellets. To avoid the loss of lithium during reactive sintering, all the green ceramic discs were covered with a sacrificial powder of the same composition and then sintered in air at 1200 °C for 20 h.<sup>42</sup>

Free-standing solid electrolyte membranes were fabricated using the solution casting technique, as illustrated in Figure S1 (Supplementary Material). Initially, a predetermined amount of PVDF-HFP was added to the DMF solvent. LiTFSI (wt. ratio of P(VDF-HFP):LiTFSI :: 2.5:1) was then added to the mixture and stirred continuously for 6 h to make a homogeneous slurry. In the next

step, Y-LZP powder was added and stirred for an additional 12 hours. The final slurry was then drop-cast on the glass petri dish and dried for 24 hours at 60 °C using a vacuum oven. The membrane thickness was optimized by varying the slurry amount and petri dish diameter. The ceramic polymer composite electrolytes with different ceramic content (0%, 5%, 10%, 15%, and 20%) were abbreviated as CEx, where  $x$  is the wt.% of ceramic. All the membranes were punched into discs with a diameter of 18 mm and stored in an Ar-filled glovebox with H<sub>2</sub>O and O<sub>2</sub> content <0.1 ppm.

## 2.2 Materials characterization

X-ray diffraction measurements were used to confirm the structure of Y-LZP ceramic, polymer-salt complex, and composite electrolyte (CE) membrane. XRD (Empyrean - Malvern Panalytical) was performed in  $2\theta$  range of 10-60° with a step size of  $\sim 0.01^\circ$  using monochromatic Cu-K $\alpha$  radiation. The *TOPAS Academic* (version 6) software was used to carry out the Rietveld refinements of XRD data for determining the lattice parameters and crystal density of the samples.<sup>43</sup> The experimental density of ceramic samples was measured using Archimedes' method, in which xylene (density  $\sim 0.864$  g/ml) was used as the medium. The surface morphologies of as-sintered ceramic pellets and CE membranes were recorded by a field-emission scanning electron microscope (FESEM, model JEOL-7610+) equipped with an energy-dispersive X-ray spectroscopy (EDS) analysis system. A PerkinElmer Spectrum IR (Model number: Spectrum 2) was used to obtain Fourier Transform Infrared Spectroscopy (FTIR) spectra (range: 500–1730 cm<sup>-1</sup>). The thermogravimetric analysis (TGA) was done at a 5 °C/min heating rate to measure mass changes with temperature using a PerkinElmer Simultaneous Thermal Analyzer instrument (model number: STA 8000). The surfaces of the ceramic pellets were coated with a thin layer of Ag paste to ensure good electrical contact. The impedance measurements of

electroded pellets and CE membranes positioned between two stainless-steel electrodes were measured in a frequency range of 1 Hz to 1 MHz using an LCR meter (Make: NF Corp., ZM2376). The obtained impedance data were fitted using the EIS analyzer.<sup>44</sup> Using the Keithley Source Meter Unit (model 2450-EC), Linear sweep voltammetry (LSV) measurement was carried out. The LSV was performed at a scanning rate of  $0.1 \text{ mV s}^{-1}$  over a potential range of 1.5–5.8 V.

For the electrochemical property, various coin cells of CR2032-type (Li|CE15|Li, Li|CE15|SS, and a full Li|CE15|LiMn<sub>2</sub>O<sub>4</sub> cell) were fabricated using CE15 membranes with 18 mm diameter. For Li<sup>+</sup> transference number, Li|CE|Li cells were subjected to AC impedance (frequency range of 1 Hz - 1 MHz, perturbation voltage: 10 mV) measurements before and after DC polarization. Lithium plating/stripping cycling test was performed on symmetric Li|CE|Li cells at different areal current densities to observe the stability of the fabricated membranes for lithium dendrites and overpotential. To demonstrate the applicability of CE15 as the solid electrolyte in a solid-state lithium metal cell, galvanostatic charge-discharge measurements were carried out on a Li|CE15|LiMn<sub>2</sub>O<sub>4</sub> cell at 0.1C. LiMn<sub>2</sub>O<sub>4</sub> (LMO) (coated on one side of aluminum foil with an active material density of  $\sim 16.6 \text{ mg/cm}^2$  with a rated specific capacity of  $\sim 110 \text{ mAh/g.}$ ) was purchased from MTI Corporation. The XRD pattern of the as-received LMO cathode is displayed in Figure S2.

### **3. Results and discussions**

#### **3.1 XRD analysis**

The powder XRD pattern of the Y-LZP sample prepared at 1200 °C is shown in Figure 1(a). It is to be noted that no rhombohedral phase was observed in samples heated at temperatures below 1200 °C. The open circle symbols show the observed XRD pattern, whereas the solid violet line is the Rietveld refined profile. The difference curve is indicated by the gray line, and olive vertical

bars represent calculated Bragg's peak positions for the space group  $R\bar{3}c$ . All major peaks in the XRD pattern fit the rhombohedral phase. An 8-order polynomial function was employed to fit the background in the XRD pattern, while the pseudo-Voigt II function was applied to refine the peak profile with an asymmetry correction based on axial divergence. The minor impurity peaks observed in Figure 1(a) were identified as belonging to the  $Y\text{P}_3\text{O}_9$ .<sup>45</sup> The calculated lattice parameters were observed to be  $a = b = 8.8820(5) \text{ \AA}$  and  $c = 22.2359(12) \text{ \AA}$ , with a volume of  $1519.18(14) \text{ \AA}^3$ . The refined atomic coordinates, occupancy, and Wyckoff positions for Y-LZP are given in Table 1. The volume of rhombohedral  $\text{LiZr}_2(\text{PO}_4)_3$  is reported to be around  $1509 \text{ \AA}^3$ .<sup>13</sup> The increase in the unit cell volume of Y-LZP over LZP can be attributed to the octahedrally coordinated 10% of  $\text{Zr}^{4+}$  ( $0.72 \text{ \AA}$ ) being replaced by larger  $\text{Y}^{3+}$  ( $0.90 \text{ \AA}$ ) and increased Li concentration in Y-LZP.<sup>46</sup>

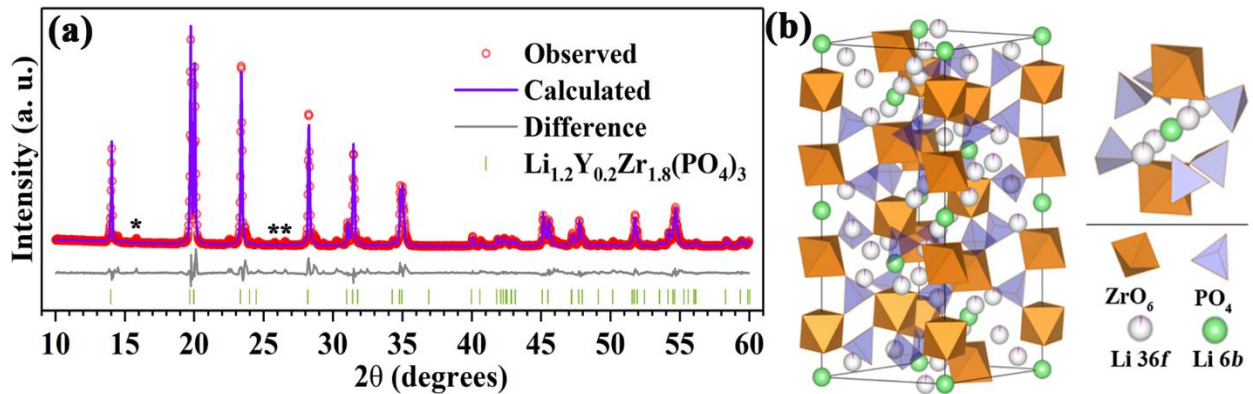


Figure 1. (a) XRD pattern of typical Rietveld refinement profile for Y-LZP (open red circle) sample calcined at  $1200 \text{ }^\circ\text{C}$ . Stars (\*) represent impurity peaks of minor  $Y\text{P}_3\text{O}_9$  phase. Calculated (violet solid line), difference (grey solid line) & Bragg's peak positions (olive vertical lines) in XRD plot and (b) Y-LZP crystal structure and the arrangement of ions & polyhedra around the Li 6b site.

In a rhombohedral NASICON structure, lithium-ion conduction occurs through 3D tunnels. The crystal structure of NASICON-type Y doped- $\text{LiZr}_2(\text{PO}_4)_3$  is shown in Figure 1(b). This structure comprises  $\text{ZrO}_6$  and  $\text{PO}_4$  polyhedra, which are corner-shared to form a 3D network structure accommodating lithium. There are two different types of Li-ion sites (Li1-6b, Li2-36f) in which

the 6b sites are fully filled, as displayed in Figure 1(b). 36f sites, which are split around the 6b site, are partially occupied by the Li-ions, as shown in Figure 1(b). The crystallographic parameters which are presented in the Table 1 was used to imagine Li<sup>+</sup> migration pathway via Chen and Adams's softBV software.<sup>43, 47, 48</sup> Figure S3 displays the BVPA software's output plotted using the VESTA software.<sup>48</sup> This figure demonstrates three-dimensionally interconnected Li<sup>+</sup> migration routes in Y-LZP.

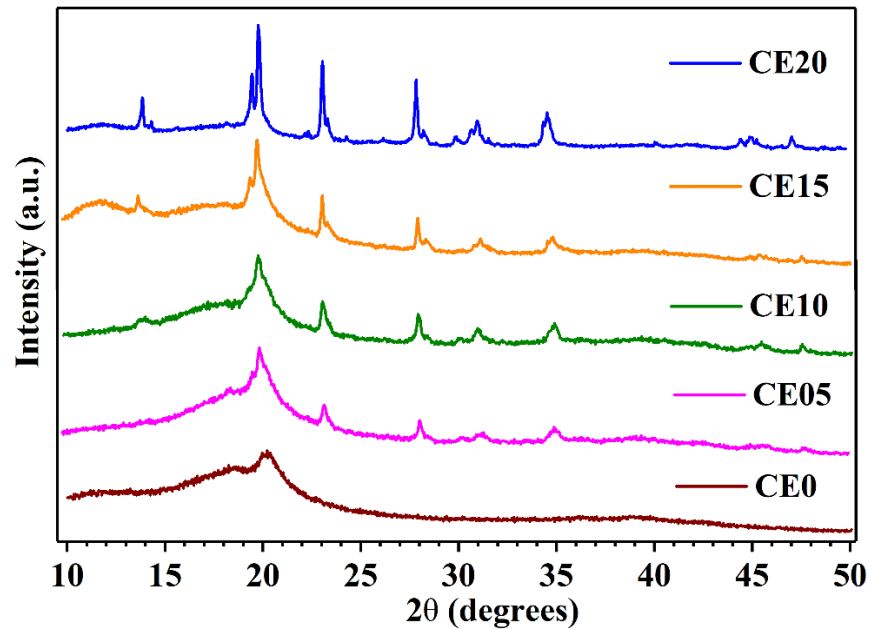


Figure 2. XRD patterns of  $CEx$  ( $x = 0, 5, 10, 15, \text{ and } 20$ ).

XRD patterns of composite membranes with different weight fractions of Y-LZP as ceramic fillers in the polymer P(VDF-HFP) + LITFSI matrix are displayed in Figure 2. A broad peak centered around at  $2\theta \approx 20^\circ$  for CE0 (i.e., P(VDF-HFP) + LITFSI) denotes the presence of semi-crystallinity of P(VDF-HFP).<sup>49</sup> The XRD pattern for CE05 shows peaks corresponding to the rhombohedral Y-LZP phase, which becomes more noticeable as the amount of ceramic filler increases. The absence of new peaks in these XRD patterns indicates that the P(VDF-HFP) polymer matrix and Y-LZP filler are compatible.

**Table 1:** Various crystallographic parameters obtained from the Rietveld refinement of room temperature powder XRD data of  $\text{Li}_{1.2}\text{Y}_{0.2}\text{Zr}_{1.8}(\text{PO}_4)_3$  sample sintered at 1200 °C for 20 h.

Site	Wyckoff symbols	x	y	z	Elements	Occupancy
<b>Li1</b>	6b	0	0	0	Li <sup>+1</sup>	1
<b>Li2</b>	36f	0	0.25	0.05	Li <sup>+1</sup>	0.033
<b>Zr</b>	12c	0	0	0.14	Zr <sup>+4</sup>	0.9
<b>Y</b>	12c	0	0	0.14	Y <sup>+3</sup>	0.1
<b>P</b>	18e	0.29	0	0.25	P <sup>+5</sup>	1
<b>O1</b>	36f	0.17	0.98	0.19	O <sup>-2</sup>	1
<b>O2</b>	36f	0.19	0.17	0.08	O <sup>-2</sup>	1

### 3.2 Microstructural analysis

Figure 3(a) displays the representative FESEM micrograph of the as-sintered ceramic pellet. The relative density remains at ~ 90% of the theoretical density. The micrograph reveals a few inter-grain microcracks. The anisotropic thermal shrinkage of the sintered pellet during cooling from high-temperature sintering is known to cause these microcracks in many NASICON-type materials<sup>50-54</sup>. The fractured surface of the pellet in Figure 3(b) shows densely packed and randomly oriented grains of a wide grain size distribution (an average grain size of  $10 \pm 5 \mu\text{m}$ ). Figure 3(c) shows an SEM micrograph of the CE15 electrolyte membrane. Figs. 3(d)-3(l) confirm that various constituent elements (Y, Zr, P, S, C, N, F, and O) are distributed uniformly throughout the sample.

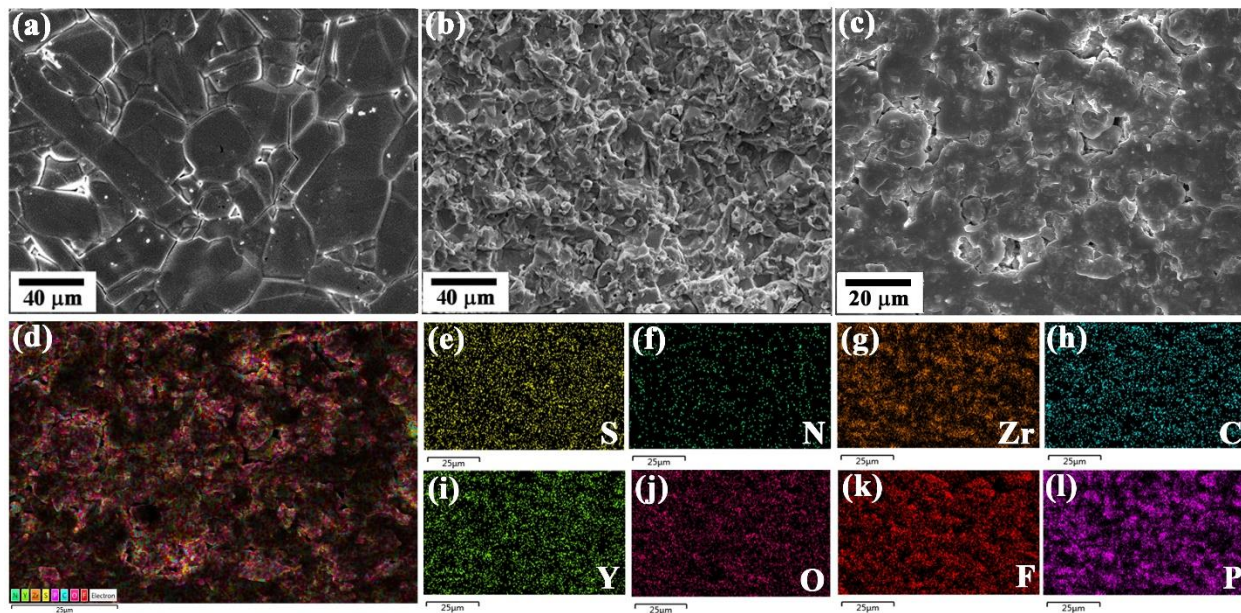


Figure 3. SEM micrographs of (a) Y-LZP, (b) Cross-section of fractured Y-LZP, (c) CE15 film, and (d)-(l) EDS elemental mapping of CE15 membrane.

The SEM images of CE10 and CE20 are given in Figure S4(a) and Figure S4(b), respectively. The increase in Y-LZP particle aggregation is noticeable in the CE20 membrane, which could be detrimental to facile  $\text{Li}^+$  conduction in the polymer-ceramic composite electrolyte due to the higher grain boundary resistance, as discussed later in the next section.

### 3.3 Fourier Transform Infrared Spectroscopy (FTIR) analysis

To investigate the modification of the bond structure resulting from the incorporation of ceramic filler into the polymer matrix, FTIR spectroscopy was conducted. The resulting FTIR spectra (in the  $500 - 1730 \text{ cm}^{-1}$  range) of Y-LZP, CE0, and CE15 samples are displayed in Figure 4. The peak at  $625 \text{ cm}^{-1}$  in the FTIR spectrum of the Y-LZP ceramic corresponds to the M-O bonds in the octahedra of Y-LZP. The additional peaks in the spectrum are attributed to the P-O stretching vibration modes located at  $560$  and  $943 \text{ cm}^{-1}$ . The band corresponding to the rocking vibrations of  $\text{CH}_2$  in PVDF-HFP (CE0) is centered around  $840 \text{ cm}^{-1}$ . The band at  $1264 \text{ cm}^{-1}$  represents the

asymmetric stretching of  $\text{CF}_2$ , C–C symmetric stretching, and the scissoring vibration of C–C–C bonds.

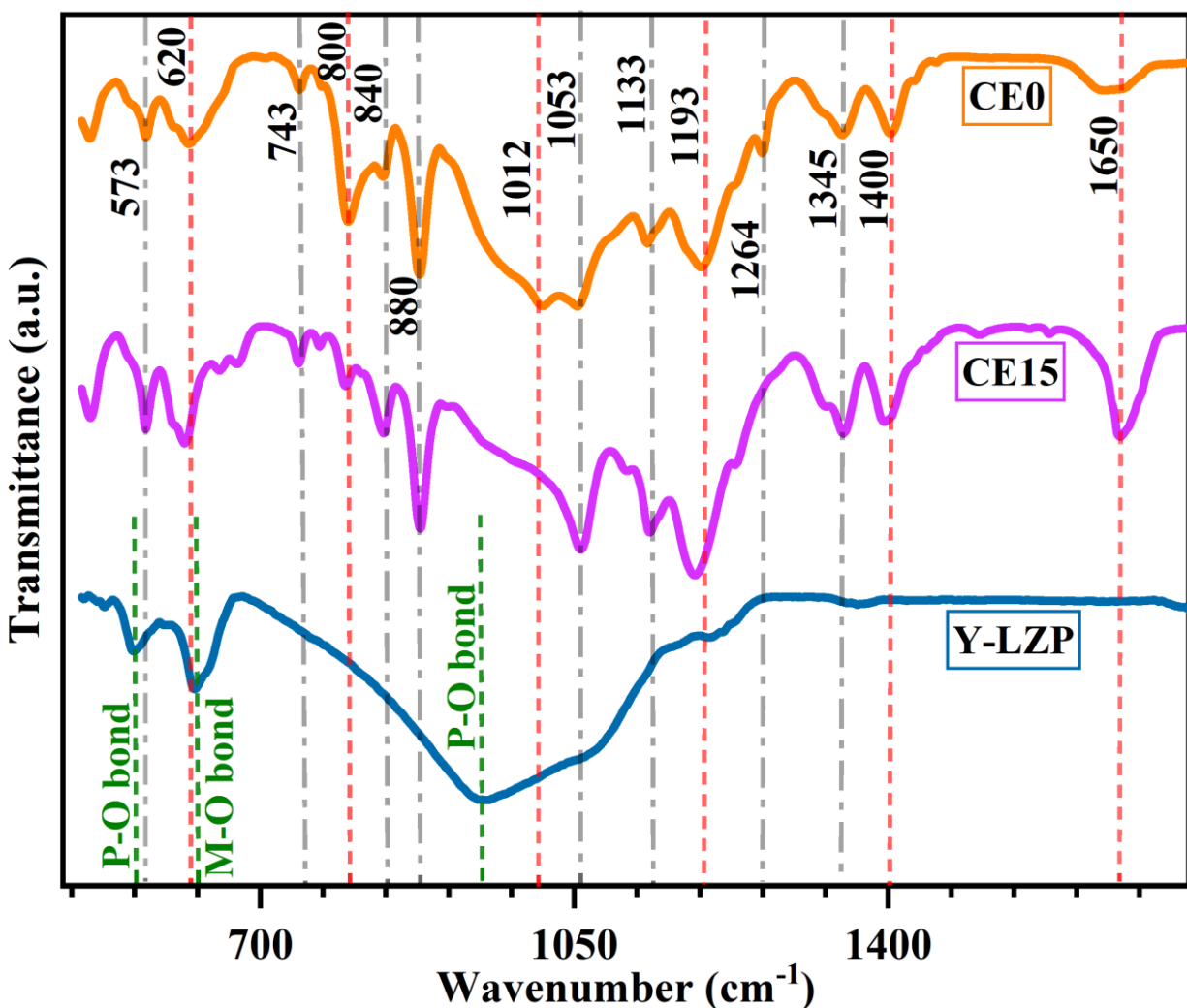


Figure 4. FTIR spectra of CE0, CE15. And Y-LZP ceramic.

The peak at  $1400\text{ cm}^{-1}$  is due to the wagging vibrations of  $\text{CH}_2$  bonds and the asymmetric stretching of C–C bonds.<sup>55</sup> The mixed modes of molecular vibrations, which include a combination of -C-C and - $\text{CF}_2$  symmetric stretching as well as C-F symmetric stretching vibrations, are shown by the transmittance peaks at about  $880$  and  $1193\text{ cm}^{-1}$ , respectively.<sup>56-58</sup> The emergence of a new peak at  $\sim 573\text{ cm}^{-1}$  (in FTIR spectra of CE0 and CE15) is ascribed to LiTFSI salt's asymmetric -

CF<sub>3</sub> bending vibrations. Free TFSI<sup>-</sup> is indicated by a peak in the FTIR spectra at about 743 cm<sup>-1</sup>.<sup>59</sup> Peaks at 1053, 1133, 1012, and 1345 cm<sup>-1</sup> result from C-H stretching. The inclusion of ceramic into the polymer matrix could be the cause of a minor change in the C-F stretching and C-H bending peaks at 620 cm<sup>-1</sup> and 800 cm<sup>-1</sup>, respectively, due to Lewis acid-base interactions between TFSI<sup>-</sup> and the ceramic particles.<sup>60</sup>

### 3.4 Ionic conductivity

The Nyquist plots of the Y-LZP sintered ceramic sample and CEx ( $x = 0, 05, 10, 15, 20$ ) membranes are shown in Figure 5. An incomplete depressed semicircle at high frequencies and a semicircular arc in the intermediate frequency region are seen in the Nyquist plot of the sintered Y-LZP pellet at RT (Figure 5(a)). The existence of the slanted line in the low-frequency region denotes the ion-blocking nature of the silver electrodes. An equivalent electric circuit, shown in Figure 5(a) inset, was employed to fit the impedance data at various temperatures. The dimensions of the sintered Y-LZP pellet were 1.5 mm in thickness and a diameter of ~ 8.8 mm. It can be seen from Figure 5(a) that the overall resistance (~ 29 kΩ) of the sample is dominated by the grain boundary resistance (~ 24.5 kΩ). Such high grain boundary resistance in the sample may be due to the poor densification, microcracks, and impurity phase segregation at grain boundaries.<sup>13, 61-63</sup> The lithium-ion conductivity in NASICON-type electrolytes is affected by grain boundary and intra/inter grain microcracks, which prevent the rapid movement of lithium ions between the grains. Furthermore, it is well-recognized that the microcracks found in this specimen negatively affect the lithium-ion conductivity.<sup>50, 64</sup>

The fitted resistance values and the samples' dimensions were used to calculate the temperature-dependent conductivity. The calculated total, grain, and grain boundary conductivities of the Y-LZP pellet at room temperature (25 °C) are  $8.51 \times 10^{-6} \text{ S cm}^{-1}$ , and  $5.31 \times 10^{-5} \text{ S cm}^{-1}$ , and  $1 \times$

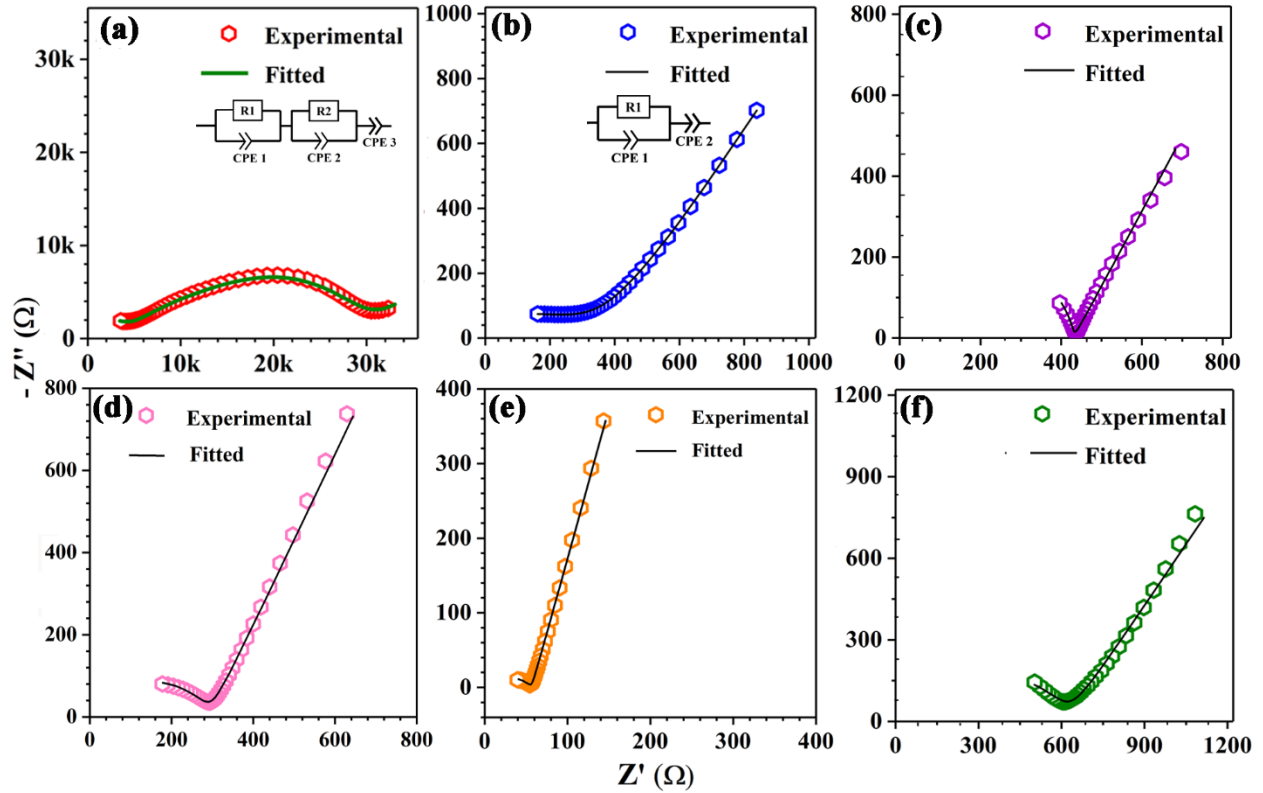


Figure 5. Nyquist plot of (a) sintered ceramic pellet, (b) CE0 membrane, (c) CE05 membrane, (d) CE10 membrane, (e) CE15 membrane, and (f) CE20 membrane. Inset-(a) shows equivalent circuit for sintered ceramic pellet and inset-(b) shows equivalent circuit used fitting the impedance data for CEx ( $x = 0, 05, 10, 15, 20$ ) membranes.

$10^{-5} \text{ S cm}^{-1}$ , respectively. This observed RT grain conductivity in our sample is much higher than those reported for undoped  $\text{LiZr}_2(\text{PO}_4)_3$  ( $8 \times 10^{-7} \text{ S cm}^{-1}$ ) and is in the range reported for Ca-doped LZP ( $4.9 \times 10^{-5} \text{ S cm}^{-1}$ ), Sr-doped LZP ( $3.4 \times 10^{-5} \text{ S cm}^{-1}$ ), and Al-doped LZP ( $2.77 \times 10^{-5} \text{ S cm}^{-1}$ ) samples.<sup>13, 65, 66</sup> The partial replacement of  $\text{Zr}^{4+}$  with  $\text{Y}^{3+}$  enlarges the migration channels inside the NASICON lattice and increases the  $\text{Li}^+$  concentration. Accordingly, faster ionic conduction is facilitated in the bulk of Y-LZP.

In the Nyquist plots of CEx ( $x = 0, 5, 10, 15, \text{ and } 20$ ), a partial semicircular arc and a tail-like feature are observed (Figure 5 (b-f)). The response from the bulk is typically a semi-circular arc in the high-frequency region, while the tail is due to the  $\text{Li}^+$ -blocking nature of the stainless-steel

electrodes. The equivalent circuit, which consists of a constant phase element CPE2 connected in series with another parallel combination of CPE1 and resistor R1, was used to fit the complex impedance data to estimate the conductivity of CEx samples as shown Figure 5(b) inset. Using the sample dimensions and the fitted values of R1, the conductivity of all prepared composites was determined (Table 2).

**Table 2:** Values of the total conductivity of different membranes at room temperature.

CEx	Resistance R1 ( $\Omega$ )	Thickness (mm)	Total conductivity ( $S\text{ cm}^{-1}$ )
CE0	350	0.05	$5.62 \times 10^{-6}$
CE05	430	0.06	$5.48 \times 10^{-6}$
CE10	290	0.06	$8.13 \times 10^{-6}$
CE15	56	0.06	$5.78 \times 10^{-5}$
CE20	626	0.08	$5.02 \times 10^{-6}$

The room temperature total conductivity was found to increase gradually from  $5.52 \times 10^{-6} S\text{ cm}^{-1}$  for the sample with  $x = 5$  to  $5.78 \times 10^{-5} S\text{ cm}^{-1}$  for the sample with  $x = 15$  as ceramic concentration increased; however, conductivity decreased again to  $5.06 \times 10^{-6} S\text{ cm}^{-1}$  for CE20 sample. The low conductivity observed for the CE0 sample is due to the slow ionic motions in the crystalline phase of PVDF-HFP (see Figure 5(b)). The semi-crystallinity of the polymer matrix is known to diminish when ceramic powders are added to polymers, and  $Li^+$  conduction in the amorphous phase is more facile in comparison to that of the crystalline phase.<sup>67, 68</sup> Lewis acid-base interaction develops the interfacial (space charge) polarization zone at the contact of polymer matrix and ceramic particles, boosting the  $Li^+$  conduction.<sup>69</sup> However, ceramic content increment gives rise to the agglomeration that impedes  $Li^+$  conduction via the polymer matrix.<sup>70</sup> It should be mentioned that even after

heating at 50–80 °C in vacuum, the DMF solvent has reportedly been shown to be present in PVDF-based electrolyte. The enhanced lithium-ion conduction in PVDF-based electrolytes is demonstrated to be a result of the Li<sup>+</sup>-DMF complex. Such complexes might contribute to observed Li<sup>+</sup> conduction in P(VDF-HFP)-based electrolytes prepared in this study.<sup>60, 71</sup> The thermogravimetric data and its corresponding differential TGA (D-TGA) curve of the solid CE membrane are given in Figure S5. There seems to be a small decrease (~ 3%) in the weight of the sample even below 200 °C. The D-TGA curve also shows two small valleys below 200 °C (Figure S5(b) inset), which could be due to the evaporation of absorbed moisture and that of the organic solvent, i.e., DMF. The decomposition of PVDF-HFP is reflected as the step-like decrease in the TGA curve between 300 and 450 °C.

Further, impedance measurements were carried out for all the samples at different temperatures, and the temperature-dependent conductivity was found to follow the Arrhenius equation:

$$\sigma(T) = \sigma_0 e^{\left(\frac{-E_A}{k_B T}\right)} \quad (1)$$

where  $\sigma_0$  is a pre-exponential factor,  $E_A$  is the activation energy,  $k_B$  is the Boltzmann constant, and  $T$  is the absolute temperature. The activation energies of grain conduction in the composite CE15 sample and for the ceramic pellet, estimated from the linear fitting of temperature-dependent conductivity using Eq. (1), are  $0.43 \pm 0.02$  eV and  $0.30 \pm 0.01$  eV, respectively (Figures S6(a) and 6(b)).

### 3.5 Li-ion Transference Number and Linear Sweep Voltammetry

Chronoamperometry profiles of D-LZP (see Figure S7) and CE15 (see Figure 6(a)) are displayed. As displayed in Figure S7, the Y-LZP has a very high lithium-ion migration number ~ 0.96. The lithium-ion transference number ( $t_{Li^+}$ ) for the CE15 sample was estimated using the Bruce-Vincent

method.<sup>72</sup> The test result for CE15, conducted at RT (25 °C), is displayed in Figure 6 (a). A voltage of 50 mV was applied for the DC polarization. The exponential decrement in the initial current ( $I_0$ ) (at  $t = 0$  s) value from  $\sim 11.2 \mu\text{A}$  to a steady state current ( $I_{SS}$ ) value  $\sim 7.2 \mu\text{A}$  (time  $t \approx 5000$  s) was observed in the membrane. Figure 6(a) inset displays the EIS plots for the Li|CE15|Li after and before DC polarization. The bulk resistance of the composite electrolyte is provided by the high-frequency intercept, while the overall cell resistance is provided by the intercept at the low-frequency region. The interfacial resistance (i.e., total resistance – bulk resistance) increased from  $35 \Omega$  to  $102 \Omega$  after DC polarization, and there was no discernible change in the bulk resistance. Equation (2) provides the formula for determining the lithium-ion transference number.

$$t_{\text{Li}^+} = \frac{I_{SS}(\Delta V - I_0 R_0)}{I_0(\Delta V - I_{SS} R_{SS})} \quad (2)$$

$R_0$  and  $R_{SS}$  are the interfacial resistance before and after polarization, respectively. The lithium-ion transference number was calculated to be  $\sim 0.64$  for CE15. It has been observed that a high  $t_{\text{Li}^+}$  suppressed the formation of Li dendrites by promoting a uniform  $\text{Li}^+$  deposition and decreasing concentration polarization within the electrolyte.<sup>73, 74</sup> The interplay of several factors could explain the high  $t_{\text{Li}^+}$  of CE15. Firstly, the PVDF-HFP had more amphoteric areas that encouraged LiTFSI dissociation and raised the amount of free  $\text{Li}^+$ , improving  $\text{Li}^+$  mobility.<sup>75</sup> Secondly, the high lithium-ion conducting Y-LZP component increases the  $\text{Li}^+$  conductivity by decreasing the PVDF-HFP matrix's degree of crystallinity, and the third is via the polymer/ceramic interface region.<sup>76, 77</sup> Ceramic fillers also hinder the movement of  $(\text{TFSI})^-$  and poly-ions [consisting of  $\text{Li}^+$  and  $(\text{TFSI})^-$ ] due to their larger sizes compared to  $\text{Li}^+$ . Thus, the addition of ceramics enhances the lithium-ion transference number. Table S1 provides the lithium-ion transference numbers of CEx with different fractions of ceramic filler.

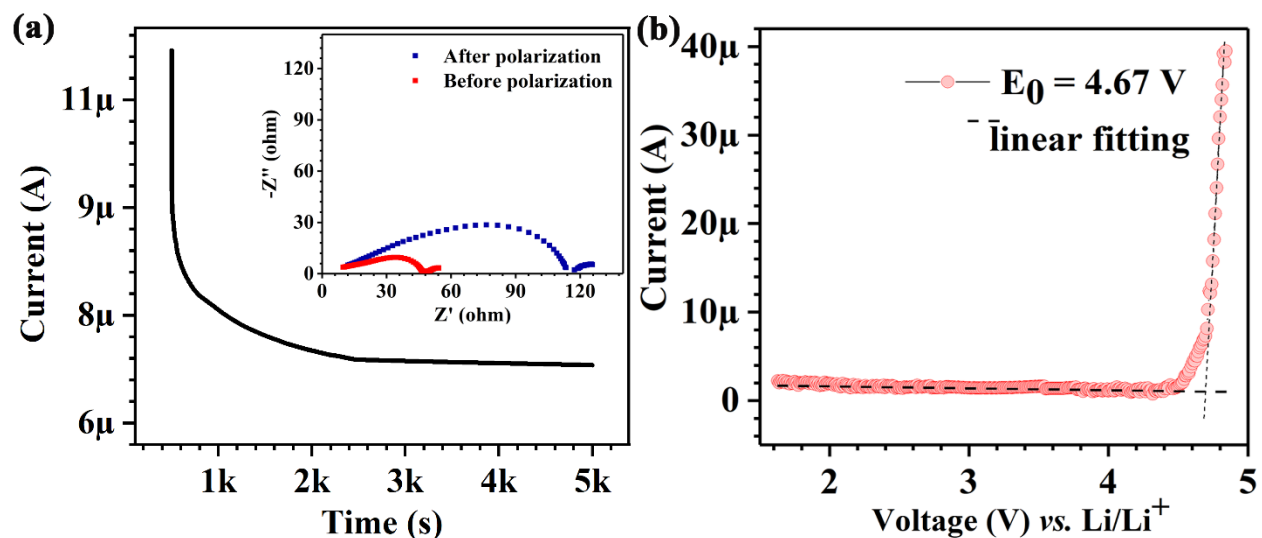


Figure 6. (a) Chronoamperometry profile of Li/CE15/Li with the inset representing the impedance data before and after DC polarization and (b) LSV curve with a scan rate of 0.1 mV/s of Li/CE15/SS.

Using linear sweep voltammetry, the electrochemical window of the composite solid electrolyte containing 15% Y-LZP powder was examined, and the result is depicted in Figure 6(b). The CE15 membrane had an electrochemical window up to a voltage of  $\sim 4.67$  V vs. Li/Li<sup>+</sup>. Anion oxidation is linked to the electrochemical stability of solid electrolytes, and a high anionic concentration can cause the breakdown of the electrolyte membrane.<sup>78</sup> The higher electrochemical stability window of 15% Y-LZP/P(VDF-HFP)/LiTFSI membrane was presumably caused by the higher stability of Y-LZP. Meanwhile, amphoteric P(VDF-HFP) regions, which prevented TFSI-anions from entering the electrode surface by anchoring them, could be partially responsible for the same.<sup>75</sup>

### 3.6 Galvanostatic charge-discharge behavior

The suppression of lithium dendrite formation and growth during the lithium plating/stripping cycle depends on the long-term interfacial stability between the lithium-metal anode and the solid electrolyte. Figure 7(a) shows the lithium plating (for 1 h) and stripping (for 1 h) cycling behavior of the symmetrical Li|CE15|Li cell at 0.1 mA cm<sup>-2</sup> current density for over 400 cycles. The symmetric cell shows an overpotential of  $\sim 200$  mV, as illustrated in Figure 7(a) inset. The similar

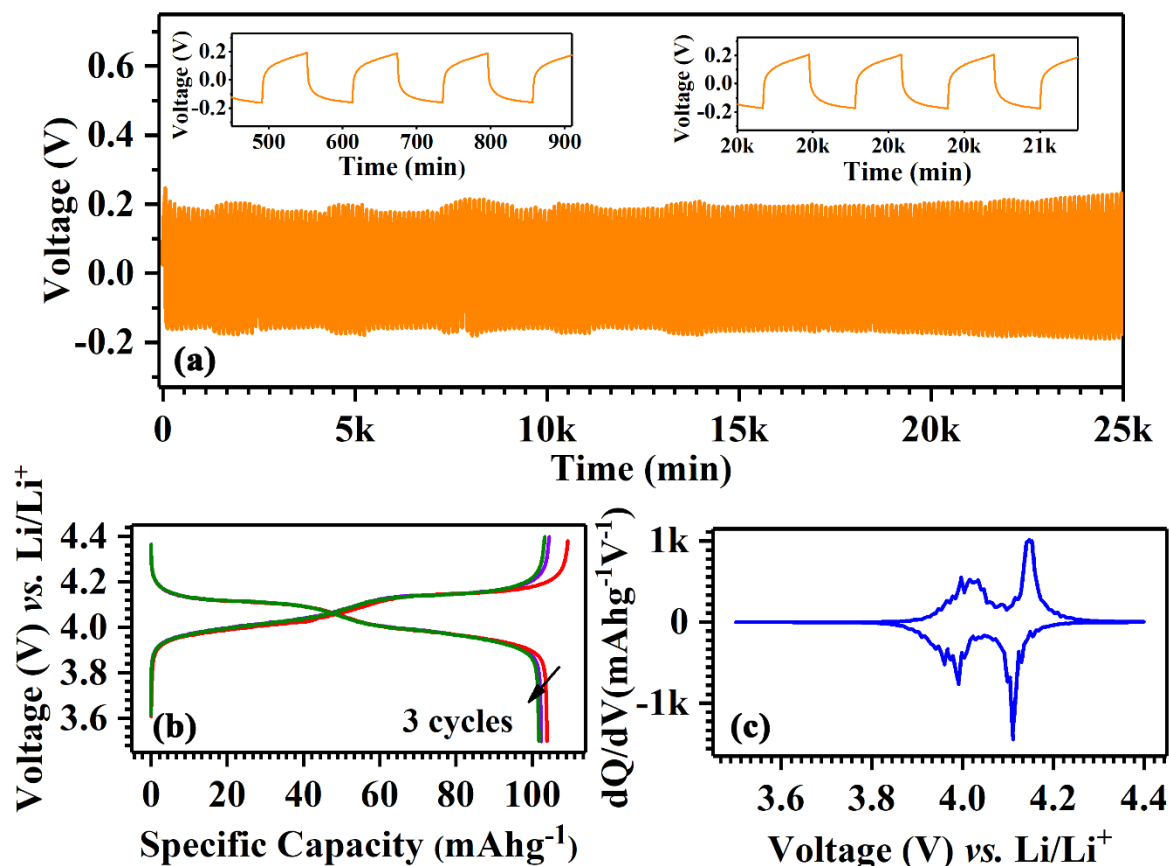


Figure 7. (a) Room temperature galvanostatic cycling profile of Li/CE15/Li cell at  $0.1 \text{ mA cm}^{-2}$ , (b) electrochemical behavior of Li/CE15/LiMn<sub>2</sub>O<sub>4</sub> cell at 0.1C, and (c) (dQ/dV) vs. voltage plot of Li/CE15/LiMn<sub>2</sub>O<sub>4</sub> at 0.1C.

values of the overpotential over 400 GCD cycles suggest relatively good compatibility and interface stability between the lithium anode and CE15. The addition of ceramic material in the polymer electrolyte improved interfacial stability between the solid electrolyte and lithium metal anode, as the ceramic particles are reported to hinder the reactions between the polymer PVDF-HFP and the lithium anode.<sup>36, 37, 79</sup> To demonstrate the use of CE15 as solid electrolytes in a full cell, a few cycles of the GCD profile of Li/CE15/LiMn<sub>2</sub>O<sub>4</sub> at 0.1C are presented in Figure 7(b). The battery provided a specific capacity value of 104 mAh/g at 0.1C (the rated capacity of LiMn<sub>2</sub>O<sub>4</sub> is 110 mAh/g at 0.1C). In the differential capacity (dQ/dV) vs. V plot of the Li/CE15/LMO cell (see Figure 7(c)), peaks demonstrate the intercalation-deintercalation potential

of the  $\text{LiMn}_2\text{O}_4$  cathode. The intercalation of lithium from the spinel structure of this cathode is represented by the peaks at  $\sim 3.96$  V and  $\sim 4.15$  V, whereas the deintercalation potentials of lithium into the LMO structure are at  $\sim 4.03$  V and  $\sim 4.18$  V. The galvanostatic charge/discharge curves of  $\text{Li}|\text{CE15}|\text{LiMn}_2\text{O}_4$  cell at various C-rates are shown in Figure 8. As can be shown from the figure, the specific capacity decreased from 104 mAh/g (at 0.1C) to  $\sim 90$  mAh/g,  $\sim 70$  mAh/g and  $\sim 50$  mAh/g at 0.5C, 1C and 2C, respectively. The drastic decrease in the specific capacity at higher C-rates could be attributed to the sluggish migration of Li-ions across the electrode-electrolyte interface at room temperature, resulting in significant overpotential at higher current densities.

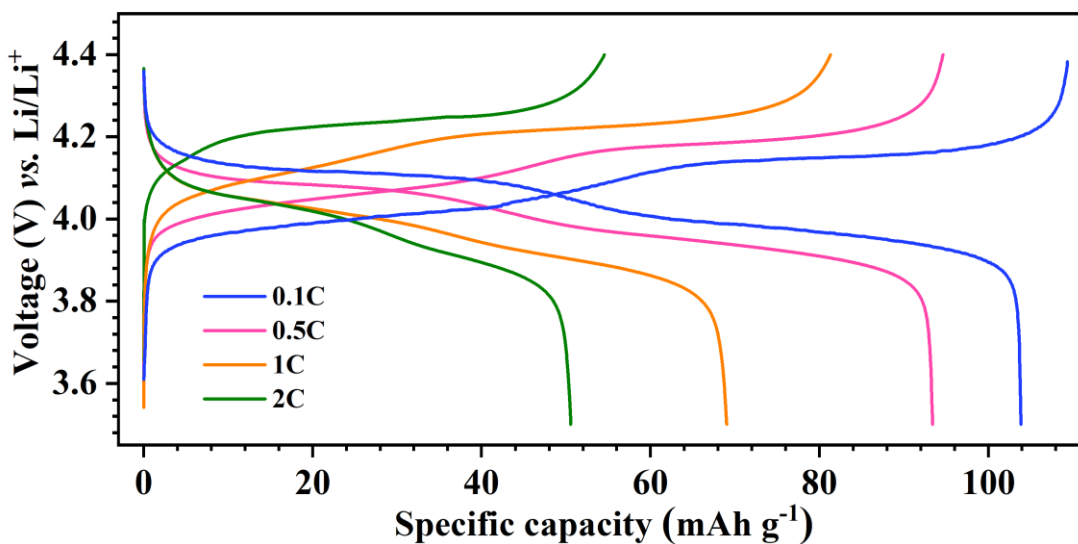


Figure 8: GCD curve at different C-rate.

#### 4. Conclusions

Flexible solid Y-LZP/P(VDF-HFP)/LITFSI electrolyte membranes (thickness  $\sim 60$   $\mu\text{m}$ ) with various compositions were fabricated *via* solution-casting method. The NASICON structure of Y-LZP was maintained in CE electrolyte membranes. A composite electrolyte membrane containing 15 wt.% of Y-LZP showed the highest RT conductivity  $\sim 5.78 \times 10^{-5}$   $\text{S cm}^{-1}$  and a lithium-ion transference number of 0.64. Adding ceramic particles enhanced the electrochemical stability

window ( $\sim 4.67$  V) of the CE15 membrane. CE15 membrane demonstrated excellent electrochemical stability in a lithium symmetric cell over 400 cycles of 2 h plating/stripping. The Li|CE15|LiMn<sub>2</sub>O<sub>4</sub> cell conveyed a discharged specific capacity of 104 mAh/g at 0.1C at RT. These findings suggest that CE membranes with P(VDF-HFP) polymer matrix and Y-LZP ceramic powder integration are promising for all-solid-state lithium batteries.

### Supporting Information

- Schematic of composite electrolyte preparation and XRD pattern of coated LiMn<sub>2</sub>O<sub>4</sub> electrode.
- Li-ion migration pathways in NASICON-type Li<sub>1.2</sub>Y<sub>0.2</sub>Zr<sub>1.8</sub>(PO<sub>4</sub>)<sub>3</sub>.
- SEM images, TGA, and Arrhenius fittings of different samples.
- Chronoamperometry profile.
- Table of Li-ion transference numbers of different samples.

### Author Contributions

**Pratiksha Gami:** Writing – review & editing, Conceptualization, Data curation, Methodology.

**Manish Badole:** XRD & SEM measurements. **Hari Narayanan Vasavan:** Writing – review & editing. **Asish Kumar Das:** Writing – review & editing. **Samridhhi Saxena:** Writing – review & editing. **Sunil Kumar:** Funding acquisition, Conceptualization, Supervision, Conceived the idea and supervised the work.

### Notes

The authors declare no competing financial interests.

### Acknowledgments

The authors thank the Science and Engineering Research Board (SERB) for the Core Research Grant (Grant no. CRG/2021/005548). Department of Science and Technology (DST), Government of India is also gratefully acknowledged for funding (Grant no. DST/TMD/IC-MAP/2K20/01).

## References

1. Baktash, A.; Reid, J. C.; Yuan, Q.; Roman, T.; Searles, D. J., Shaping the Future of Solid-State Electrolytes through Computational Modeling. *Adv. Mater.* **2020**, *32* (18), 1908041, <https://doi.org/10.1002/adma.201908041>.
2. Li, Y.; Wang, J.; Zhou, Z.; Deng, J.; Yao, Q.; Chu, H.; Wang, Z.; Sun, L.; Zhou, H., Large-scale synthesis of porous  $\text{Li}_3\text{V}_2(\text{PO}_4)_3$ @C/AB hollow microspheres with interconnected channel as high performance cathodes for lithium-ion batteries. *J. Alloys Compd.* **2019**, *774*, 879-886, <https://doi.org/10.1016/j.jallcom.2018.09.214>.
3. Kang, K.; Meng, Y. S.; Bréger, J.; Grey, C. P.; Ceder, G., Electrodes with high power and high capacity for rechargeable lithium batteries. *Science* **2006**, *311* (5763), 977-80, <https://doi.org/10.1126/science.1122152>.
4. Yang, C.; Fu, K.; Zhang, Y.; Hitz, E.; Hu, L., Protected Lithium-Metal Anodes in Batteries: From Liquid to Solid. *Adv. Mater.* **2017**, *29* (36), 1701169, <https://doi.org/10.1002/adma.201701169>.
5. Hu, Y.-S., Batteries: Getting solid. *Nature Energy* **2016**, *1*, 16042, <https://doi.org/10.1038/nenergy.2016.42>.
6. Shahid, S.; Agelin-Chaab, M., A review of thermal runaway prevention and mitigation strategies for lithium-ion batteries. *Energy Convers. Manage. X* **2022**, *16*, 100310, <https://doi.org/10.1016/j.ecmx.2022.100310>.

7. Fang, R.; Liu, Y.; Li, Y.; Manthiram, A.; Goodenough, J. B., Achieving stable all-solid-state lithium-metal batteries by tuning the cathode-electrolyte interface and ionic/electronic transport within the cathode. *Mater. Today* **2023**, *64*, 52-60, <https://doi.org/10.1016/j.mattod.2023.03.001>.
8. Fang, R.; Li, Y.; Wu, N.; Xu, B.; Liu, Y.; Manthiram, A.; Goodenough, J. B., Ultra-Thin Single-Particle-Layer Sodium Beta-Alumina-Based Composite Polymer Electrolyte Membrane for Sodium-Metal Batteries. *Adv. Funct. Mater.* **2023**, *33* (6), 2211229, <https://doi.org/10.1002/adfm.202211229>.
9. Liu, Y.-N.; Xiao, Z.; Zhang, W.-K.; Zhang, J.; Huang, H.; Gan, Y.-P.; He, X.-P.; Kumar, G. G.; Xia, Y., Poly(m-phenylene isophthalamide)-reinforced polyethylene oxide composite electrolyte with high mechanical strength and thermostability for all-solid-state lithium metal batteries. *Rare Metals* **2022**, *41* (11), 3762-3773, <https://doi.org/10.1007/s12598-022-02065-3>.
10. Li, S.; Zhang, S.-Q.; Shen, L.; Liu, Q.; Ma, J.-B.; Lv, W.; He, Y.-B.; Yang, Q.-H., Progress and Perspective of Ceramic/Polymer Composite Solid Electrolytes for Lithium Batteries. *Advanced Science* **2020**, *7* (5), 1903088, <https://doi.org/10.1002/advs.201903088>.
11. Kim, H.-K.; Barai, P.; Chavan, K.; Srinivasan, V., Transport and mechanical behavior in PEO-LLZO composite electrolytes. *J. Solid State Electrochem.* **2022**, *26* (9), 2059-2075, <https://doi.org/10.1007/s10008-022-05231-w>.
12. Loutati, A.; Guillon, O.; Tietz, F.; Fattakhova-Rohlfing, D., NaSICON-type solid-state Li<sup>+</sup> ion conductors with partial polyanionic substitution of phosphate with silicate. *Open Ceram.* **2022**, *12*, <https://doi.org/10.1016/j.oceram.2022.100313>.

13. Kumar, S.; Balaya, P., Improved ionic conductivity in NASICON-type  $\text{Sr}^{2+}$  doped  $\text{LiZr}_2(\text{PO}_4)_3$ . *Solid State Ion.* **2016**, *296*, 1-6, <https://doi.org/10.1016/j.ssi.2016.08.012>.
14. Hong, H. Y. P., Crystal structures and crystal chemistry in the system  $\text{Na}_{1+x}\text{Zr}_2\text{SixP}_{3-x}\text{O}_{12}$ . *Mater. Res. Bull.* **1976**, *11* (2), 173-182, [https://doi.org/10.1016/0025-5408\(76\)90073-8](https://doi.org/10.1016/0025-5408(76)90073-8).
15. Goodenough, J. B.; Hong, H. Y. P.; Kafalas, J. A., Fast  $\text{Na}^+$ -ion transport in skeleton structures. *Mater. Res. Bull.* **1976**, *11* (2), 203-220, [https://doi.org/10.1016/0025-5408\(76\)90077-5](https://doi.org/10.1016/0025-5408(76)90077-5).
16. Pareek, T.; Dwivedi, S.; Singh, B.; Kumar, D.; Kumar, P.; Kumar, S.,  $\text{LiSnZr}(\text{PO}_4)_3$ : NASICON-type solid electrolyte with excellent room temperature  $\text{Li}^+$  conductivity. *J. Alloys Compd.* **2019**, *777*, 602-611, <https://doi.org/10.1016/j.jallcom.2018.10.384>.
17. Pareek, T.; Dwivedi, S.; Badole, M.; Kumar, S., On processing structure–conductivity relations in NASICON-type  $\text{LiSn}_2(\text{PO}_4)_3$ . *Bull. Mater. Sci.* **2021**, *44* (3), 177, <https://doi.org/10.1007/s12034-021-02460-z>.
18. Stenina, I.; Novikova, S.; Voropaeva, D.; Yaroslavtsev, A., Solid Electrolytes Based on NASICON-Structured Phosphates for Lithium Metal Batteries. *Batteries* **2023**, *9* (8), <https://doi.org/10.3390/batteries9080407>.
19. Ramar, V.; Kumar, S.; Sivakkumar, S. R.; Balaya, P., NASICON-type  $\text{La}^{3+}$  substituted  $\text{LiZr}_2(\text{PO}_4)_3$  with improved ionic conductivity as solid electrolyte. *Electrochim. Acta* **2018**, *271*, 120-126, <https://doi.org/10.1016/j.electacta.2018.03.115>.
20. Subramanian, M. A.; Subramanian, R.; Clearfield, A., Lithium ion conductors in the system  $\text{AB}(\text{IV})_2(\text{PO}_4)_3$  ( $\text{B} = \text{Ti}, \text{Zr}$  and  $\text{Hf}$ ). *Solid State Ion.* **1986**, *18-19*, 562-569, [https://doi.org/10.1016/0167-2738\(86\)90179-7](https://doi.org/10.1016/0167-2738(86)90179-7).

21. Xu, H.; Wang, S.; Wilson, H.; Zhao, F.; Manthiram, A., Y-Doped NASICON-type  $\text{LiZr}_2(\text{PO}_4)_3$  Solid Electrolytes for Lithium-Metal Batteries. *Chem. Mater.* **2017**, *29* (17), 7206-7212, <https://doi.org/10.1021/acs.chemmater.7b01463>.
22. Yang, Y.; Yang, S.; Xue, X.; Zhang, X.; Li, Q.; Yao, Y.; Rui, X.; Pan, H.; Yu, Y., Inorganic All-Solid-State Sodium Batteries: Electrolyte Designing and Interface Engineering. *Adv. Mater.* **2023**, <https://doi.org/10.1002/adma.202308332>.
23. Xia, Y.; Wang, Q.; Liu, Y.; Zhang, J.; Xia, X.; Huang, H.; Gan, Y.; He, X.; Xiao, Z.; Zhang, W., Three-dimensional polyimide nanofiber framework reinforced polymer electrolyte for all-solid-state lithium metal battery. *J. Colloid Interface Sci.* **2023**, *638*, 908-917, <https://doi.org/10.1016/j.jcis.2023.01.138>.
24. Fang, R.; Xu, H.; Xu, B.; Li, X.; Li, Y.; Goodenough, J. B., Reaction Mechanism Optimization of Solid-State Li-S Batteries with a PEO-Based Electrolyte. *Adv. Funct. Mater.* **2021**, *31* (2), 2001812, <https://doi.org/10.1002/adfm.202001812>.
25. Das, A. K.; Badole, M.; Vasavan, H. N.; Saxena, S.; Gami, P.; Kumar, S., Highly conductive ceramic-in-polymer composite electrolyte enabling superior electrochemical performance for all-solid-state lithium batteries. *Ceram. Int.* **2023**, *49* (18), 29719-29728, <https://doi.org/10.1016/j.ceramint.2023.06.214>.
26. Zhang, H.; Oteo, U.; Judez, X.; Eshetu, G. G.; Martinez-Ibañez, M.; Carrasco, J.; Li, C.; Armand, M., Designer Anion Enabling Solid-State Lithium-Sulfur Batteries. *Joule* **2019**, *3* (7), 1689-1702, <https://doi.org/10.1016/j.joule.2019.05.003>.
27. Hu, J.; Wang, W.; Zhou, B.; Feng, Y.; Xie, X.; Xue, Z., Poly(ethylene oxide)-based composite polymer electrolytes embedding with ionic bond modified nanoparticles for all-solid-

state lithium-ion battery. *J. Membr. Sci.* **2019**, *575*, 200-208, <https://doi.org/10.1016/j.memsci.2019.01.025>.

28. Li, B.; Su, Q.; Yu, L.; Wang, D.; Ding, S.; Zhang, M.; Du, G.; Xu, B.,  $\text{Li}_{(0.35)}\text{La}_{(0.55)}\text{TiO}_{(3)}$  Nanofibers Enhanced Poly(vinylidene fluoride)-Based Composite Polymer Electrolytes for All-Solid-State Batteries. *ACS Appl. Mater. Interfaces* **2019**, *11* (45), 42206-42213, <https://doi.org/10.1021/acsami.9b14824>.

29. Zhang, X.; Xu, B.-Q.; Lin, Y.-H.; Shen, Y.; Li, L.; Nan, C.-W., Effects of  $\text{Li}_{6.75}\text{La}_3\text{Zr}_{1.75}\text{Ta}_{0.25}\text{O}_{12}$  on chemical and electrochemical properties of polyacrylonitrile-based solid electrolytes. *Solid State Ion.* **2018**, *327*, 32-38, <https://doi.org/10.1016/j.ssi.2018.10.023>.

30. Tamainato, S.; Mori, D.; Takeda, Y.; Yamamoto, O.; Imanishi, N., Composite Polymer Electrolytes for Lithium Batteries. *ChemistrySelect* **2022**, *7* (29), e202201667, <https://doi.org/10.1002/slct.202201667>.

31. Merrill, L. C.; Chen, X. C.; Zhang, Y.; Ford, H. O.; Lou, K.; Zhang, Y.; Yang, G.; Wang, Y.; Wang, Y.; Schaefer, J. L.; Dudney, N. J., Polymer–Ceramic Composite Electrolytes for Lithium Batteries: A Comparison between the Single-Ion-Conducting Polymer Matrix and Its Counterpart. *ACS Appl. Energy Mater.* **2020**, *3* (9), 8871-8881, <https://doi.org/10.1021/acsaem.0c01358>.

32. Oh, P.; Lee, H.; Park, S.; Cha, H.; Kim, J.; Cho, J., Improvements to the Overpotential of All-Solid-State Lithium-Ion Batteries during the Past Ten Years. *Adv. Energy Mater.* **2020**, <https://doi.org/10.1002/aenm.202000904>.

33. Li, Y.; Zhang, W.; Dou, Q.; Wong, K. W.; Ng, K. M.,  $\text{Li}_7\text{La}_3\text{Zr}_2\text{O}_{12}$  ceramic nanofiber-incorporated composite polymer electrolytes for lithium metal batteries. *J. Mater. Chem.* **2019**, *7* (7), 3391-3398, <https://doi.org/10.1039/C8TA11449H>.

34. Yu, S.; Schmohl, S.; Liu, Z.; Hoffmeyer, M.; Schön, N.; Hausen, F.; Tempel, H.; Kungl, H.; Wiemhöfer, H. D.; Eichel, R. A., Insights into a layered hybrid solid electrolyte and its application in long lifespan high-voltage all-solid-state lithium batteries. *J. Mater. Chem.* **2019**, *7* (8), 3882-3894, <https://doi.org/10.1039/C8TA11259B>.
35. Lv, F.; Wang, Z.; Shi, L.; Zhu, J.; Edström, K.; Mindemark, J.; Yuan, S., Challenges and development of composite solid-state electrolytes for high-performance lithium ion batteries. *J. Power Sources* **2019**, *441*, 227175, <https://doi.org/10.1016/j.jpowsour.2019.227175>.
36. Yadav, P.; Hosen, M. S.; Dammala, P. K.; Ivanchenko, P.; Van Mierlo, J.; Berecibar, M., Development of composite solid polymer electrolyte for solid-state lithium battery: Incorporating LLZTO in PVDF-HFP/LiTFSI. *Solid State Ion.* **2023**, *399*, 116308, <https://doi.org/10.1016/j.ssi.2023.116308>.
37. Pareek, T.; Dwivedi, S.; Ahmad, S. A.; Badole, M.; Kumar, S., Effect of NASICON-type  $\text{LiSnZr(PO}_4)_3$  ceramic filler on the ionic conductivity and electrochemical behavior of PVDF based composite electrolyte. *J. Alloys Compd.* **2020**, *824*, 153991, <https://doi.org/10.1016/j.jallcom.2020.153991>.
38. Sung, B.-J.; Didwal, P. N.; Verma, R.; Nguyen, A.-G.; Chang, D. R.; Park, C.-J., Composite solid electrolyte comprising poly(propylene carbonate) and  $\text{Li}_{1.5}\text{Al}_{0.5}\text{Ge}_{1.5}(\text{PO}_4)_3$  for long-life all-solid-state Li-ion batteries. *Electrochim. Acta* **2021**, *392*, 139007, <https://doi.org/10.1016/j.electacta.2021.139007>.
39. Rajamani, A.; Panneerselvam, T.; Abraham, S. E.; Murugan, R.; Sivaprakasam, S., Recent progress in polymer garnet composite electrolytes for solid-state lithium metal batteries. *Sustain. Energy Fuels* **2023**, *7* (14), 3185-3212, <https://doi.org/10.1039/D3SE00421J>.

40. Yu, X.; Manthiram, A., A review of composite polymer-ceramic electrolytes for lithium batteries. *Energy Storage Mater.* **2021**, *34*, 282-300, <https://doi.org/10.1016/j.ensm.2020.10.006>.
41. Ao, X.; Wang, X.; Tan, J.; Zhang, S.; Su, C.; Dong, L.; Tang, M.; Wang, Z.; Tian, B.; Wang, H., Nanocomposite with fast Li<sup>+</sup> conducting percolation network: Solid polymer electrolyte with Li<sup>+</sup> non-conducting filler. *Nano Energy* **2021**, *79*, 105475, <https://doi.org/10.1016/j.nanoen.2020.105475>.
42. Yang, L.; Tao, X.; Huang, X.; Zou, C.; Yi, L.; Chen, X.; Zang, Z.; Luo, Z.; Wang, X., Efficient Mutual-Compensating Li-Loss Strategy toward Highly Conductive Garnet Ceramics for Li-Metal Solid-State Batteries. *ACS Appl. Mater. Interfaces* **2021**, *13* (47), 56054-56063, <https://doi.org/10.1021/acsami.1c15115>.
43. Coelho, A. A., TOPAS and TOPAS-Academic: an optimization program integrating computer algebra and crystallographic objects written in C++. *J. Appl. Crystallogr.* **2018**, *51* (1), 210-218, <https://doi.org/10.1107/S1600576718000183>.
44. Ragoisha, A. S. B. a. G. A. EIS Spectrum Analyser. <http://www.abc.chemistry.bsu.by/vi/analyser>.
45. Hachani, S.; Guerbous, L., Synthesis, Luminescence, and Energy Transfer Properties of YPO<sub>4</sub>:Gd<sup>3+</sup>, Eu<sup>3+</sup> and YP<sub>3</sub>O<sub>9</sub>:Sm<sup>3+</sup>, Eu<sup>3+</sup> Phosphors. *J. Fluoresc.* **2019**, *29* (3), 665-672, <https://doi.org/10.1007/s10895-019-02377-1>.
46. Shannon, R. D.; Prewitt, C. T., Effective ionic radii in oxides and fluorides. *Acta Cryst. B* **1969**, *25* (5), 925-946, <https://doi.org/10.1107/S0567740869003220>.
47. Li, Y.; Liu, M.; Liu, K.; Wang, C.-A., High Li<sup>+</sup> conduction in NASICON-type Li<sub>1+x</sub>Y<sub>x</sub>Zr<sub>2-x</sub>(PO<sub>4</sub>)<sub>3</sub> at room temperature. *J. Power Sources* **2013**, *240*, 50-53, <https://doi.org/10.1016/j.jpowsour.2013.03.175>.

48. Chen, H.; Wong, L. L.; Adams, S., SoftBV - a software tool for screening the materials genome of inorganic fast ion conductors. *Acta Crystallogr. B Struct. Sci. Cryst. Eng. Mater.* **2019**, 75 (Pt 1), 18-33, <https://doi.org/10.1107/s2052520618015718>.
49. Croce, F.; Persi, L.; Scrosati, B.; Serraino-Fiory, F.; Plichta, E.; Hendrickson, M. A., Role of the ceramic fillers in enhancing the transport properties of composite polymer electrolytes. *Electrochim. Acta* **2001**, 46 (16), 2457-2461, [https://doi.org/10.1016/S0013-4686\(01\)00458-3](https://doi.org/10.1016/S0013-4686(01)00458-3).
50. Chakraborty, A.; Thirupathi, R.; Bhattacharyya, S.; Singh, K.; Omar, S., Mg-doped NASICON-type electrolyte for rechargeable solid-state sodium-ion batteries. *J. Power Sources* **2023**, 572, 233092, <https://doi.org/10.1016/j.jpowsour.2023.233092>.
51. Davidge, R. W., Cracking at grain boundaries in polycrystalline brittle materials. *Acta Metall.* **1981**, 29 (10), 1695-1702, [https://doi.org/10.1016/0001-6160\(81\)90004-3](https://doi.org/10.1016/0001-6160(81)90004-3).
52. Jackman, S.; Cutler, R., Effect of Microcracking on Ionic Conductivity in LATP. *J. Power Sources* **2012**, 218, 65–72, <https://doi.org/10.1016/j.jpowsour.2012.06.081>.
53. Cai, H.; Yu, T.; Xie, D.; Sun, B.; Cheng, J.; Li, L.; Bao, X.; Zhang, H., Microstructure and ionic conductivities of NASICON-type  $\text{Li}_{1.3}\text{Al}_{0.3}\text{Ti}_{1.7}(\text{PO}_4)_3$  solid electrolytes produced by cold sintering assisted process. *J. Alloys Compd.* **2023**, 939, 168702, <https://doi.org/10.1016/j.jallcom.2023.168702>.
54. Yu, S.; Mertens, A.; Gao, X.; Gunduz, D. C.; Schierholz, R.; Benning, S.; Hausen, F.; Mertens, J.; Kungl, H.; Tempel, H.; Eichel, R.-A., Influence of microstructure and  $\text{AlPO}_4$  secondary-phase on the ionic conductivity of  $\text{Li}_{1.3}\text{Al}_{0.3}\text{Ti}_{1.7}(\text{PO}_4)_3$  solid-state electrolyte. *Funct. Mater. Lett.* **2016**, 09 (05), 1650066, <https://doi.org/10.1142/S1793604716500661>.

55. Martins, P.; Lopes, A. C.; Lanceros-Mendez, S., Electroactive phases of poly(vinylidene fluoride): Determination, processing and applications. *Prog. Polym. Sci.* **2014**, *39* (4), 683-706, <https://doi.org/10.1016/j.progpolymsci.2013.07.006>.
56. Bormashenko, Y.; Pogreb, R.; Stanevsky, O.; Bormashenko, E., Vibrational spectrum of PVDF and its interpretation. *Polym. Test.* **2004**, *23*, 791-796, <https://doi.org/10.1016/j.polymertesting.2004.04.001>.
57. Gregorio Jr., R., Determination of the  $\alpha$ ,  $\beta$ , and  $\gamma$  crystalline phases of poly(vinylidene fluoride) films prepared at different conditions. *J. Appl. Polym. Sci.* **2006**, *100* (4), 3272-3279, <https://doi.org/10.1002/app.23137>.
58. Dwivedi, S.; Badole, M.; Gangwar, K.; Kumar, S., Relaxation processes and conduction behaviour in PVDF-TrFE and KNN-based composites. *Polymer* **2021**, *232*, 124164, <https://doi.org/10.1016/j.polymer.2021.124164>.
59. McGrath, L.; Jones, J.; Carey, E.; Rohan, J., Ionic Liquid Based Polymer Gel Electrolytes for Use with Germanium Thin Film Anodes in Lithium Ion Batteries. *ChemistryOpen* **2019**, *8*, 1429-1436, <https://doi.org/10.1002/open.201900313>.
60. Das, A. K.; Badole, M.; Vasavan, H. N.; Saxena, S.; Gami, P.; Deswal, S.; Kumar, P.; Kumar, S., Enhancing room temperature performance of solid-state lithium cell via a facile solid electrolyte-cathode interface design. *Mater. Today Sustain.* **2024**, *26*, 100758, <https://doi.org/10.1016/j.mtsust.2024.100758>.
61. Ladenstein, L.; Hogrefe, K.; Wilkening, H. M. R., Ionic Transport and Electrochemical Properties of NaSICON-Type  $\text{Li}_{1+x}\text{Hf}_{2-x}\text{Ga}_x(\text{PO}_4)_3$  for All-Solid-State Lithium Batteries. *ACS Appl. Energy Mater.* **2022**, *5* (7), 8823-8834, <https://doi.org/10.1021/acsaem.2c01304>.

62. Xue, W.; Yang, Y.; Yang, Q.; Liu, Y.; Wang, L.; Chen, C.; Cheng, R., The effect of sintering process on lithium ionic conductivity of  $\text{Li}_{6.4}\text{Al}_{0.2}\text{La}_3\text{Zr}_2\text{O}_{12}$  garnet produced by solid-state synthesis. *RSC Advances* **2018**, 8 (24), 13083-13088, <https://doi.org/10.1039/C8RA01329B>.
63. Liu, J.; Wang, T.; Yu, J.; Li, S.; Ma, H.; Liu, X., Review of the Developments and Difficulties in Inorganic Solid-State Electrolytes. *Materials* **2023**, 16 (6), 2510, <https://doi.org/10.3390/ma16062510>.
64. Singh, K.; Chakraborty, A.; Thirupathi, R.; Omar, S., Recent advances in NASICON-type oxide electrolytes for solid-state sodium-ion rechargeable batteries. *Ionics* **2022**, 28 (12), 5289-5319, <https://doi.org/10.1007/s11581-022-04765-3>.
65. Xie, H.; Li, Y.; Goodenough, J. B., NASICON-type  $\text{Li}_{1+2x}\text{Zr}_{2-x}\text{Ca}_x(\text{PO}_4)_3$  with high ionic conductivity at room temperature. *RSC Advances* **2011**, 1 (9), 1728-1731, <https://doi.org/10.1039/C1RA00383F>.
66. Akkinapally, B.; Reddy, I. N.; Ko, T. J.; Yoo, K.; Shim, J., Dopant effect on  $\text{Li}^+$  ion transport in NASICON-type solid electrolyte: Insights from molecular dynamics simulations and experiments. *Ceram. Int.* **2022**, 48 (9), 12142-12151, <https://doi.org/10.1016/j.ceramint.2022.01.075>.
67. Yao, P.; Yu, H.; Ding, Z.; Liu, Y.; Lu, J.; Lavorgna, M.; Wu, J.; Liu, X., Review on Polymer-Based Composite Electrolytes for Lithium Batteries. *Front. Chem.* **2019**, 7, <https://doi.org/10.3389/fchem.2019.00522>.
68. Manuel Stephan, A.; Nahm, K. S., Review on composite polymer electrolytes for lithium batteries. *Polymer* **2006**, 47 (16), 5952-5964, <https://doi.org/10.1016/j.polymer.2006.05.069>.

69. Luo, S.; Liu, X.; Gao, L.; Deng, N.; Sun, X.; Li, Y.; Zeng, Q.; Wang, H.; Cheng, B.; Kang, W., A review on modified polymer composite electrolytes for solid-state lithium batteries. *Sustain. Energy Fuels* **2022**, *6* (22), 5019-5044, <https://doi.org/10.1039/D2SE01093C>.
70. Wan, Z.; Lei, D.; Yang, W.; Liu, C.; Shi, K.; Hao, X.; Shen, L.; Lv, W.; Li, B.; Yang, Q. H.; Kang, F.; He, Y.-B., Low Resistance-Integrated All-Solid-State Battery Achieved by  $\text{Li}_7\text{La}_3\text{Zr}_2\text{O}_{12}$  Nanowire Upgrading Polyethylene Oxide (PEO) Composite Electrolyte and PEO Cathode Binder. *Adv. Funct. Mater.* **2018**, *29*, 1805301, <https://doi.org/10.1002/adfm.201805301>.
71. Zhang, X.; Wang, S.; Xue, C.; Xin, C.; Lin, Y.; Shen, Y.; Li, L.; Nan, C.-W., Self-Suppression of Lithium Dendrite in All-Solid-State Lithium Metal Batteries with Poly(vinylidene difluoride)-Based Solid Electrolytes. *Adv. Mater.* **2019**, *31* (11), 1806082, <https://doi.org/10.1002/adma.201806082>.
72. Evans, J.; Vincent, C. A.; Bruce, P. G., Electrochemical measurement of transference numbers in polymer electrolytes. *Polymer* **1987**, *28* (13), 2324-2328, [https://doi.org/10.1016/0032-3861\(87\)90394-6](https://doi.org/10.1016/0032-3861(87)90394-6).
73. Zhao, Y.; Wang, L.; Zhou, Y.; Liang, Z.; Tavajohi, N.; Li, B.; Li, T., Solid Polymer Electrolytes with High Conductivity and Transference Number of Li Ions for Li-Based Rechargeable Batteries. *Advanced Science* **2021**, *8* (7), 2003675, <https://doi.org/10.1002/advs.202003675>.
74. Chen, L.; Li, W.; Fan, L.-Z.; Nan, C.-W.; Zhang, Q., Intercalated Electrolyte with High Transference Number for Dendrite-Free Solid-State Lithium Batteries. *Adv. Funct. Mater.* **2019**, *29* (28), 1901047, <https://doi.org/10.1002/adfm.201901047>.

75. Yu, Y.; Sun, N.; Wu, A.; Lu, F.; Zheng, L., Zwitterion-containing electrolytes with semi-crystalline PVDF-Co-HFP as a matrix for safer lithium-ion batteries. *J. Mol. Liq.* **2019**, *282*, 340-346, <https://doi.org/10.1016/j.molliq.2019.03.027>.
76. Chen, F.; Yang, D.; Zha, W.; Zhu, B.; Zhang, Y.; Li, J.; Gu, Y.; Shen, Q.; Zhang, L.; Sadoway, D. R., Solid polymer electrolytes incorporating cubic  $\text{Li}_7\text{La}_3\text{Zr}_2\text{O}_{12}$  for all-solid-state lithium rechargeable batteries. *Electrochim. Acta* **2017**, 1106-1114, <https://doi.org/101016/j.electacta201711164>.
77. Lu, J.; Liu, Y.; Yao, P.; Ding, Z.; Tang, Q.; Wu, J.; Ye, Z.; Huang, K.; Liu, X., Hybridizing Poly(vinylidene fluoride-co-hexafluoropropylene) with  $\text{Li}_{6.5}\text{La}_3\text{Zr}_{1.5}\text{Ta}_{0.5}\text{O}_{12}$  as a Lithium-Ion Electrolyte for Solid State Lithium Metal Batteries. *Chem. Eng. J.* **2019**, *367*, <https://doi.org/10.1016/j.cej.2019.02.148>.
78. Shin, J. H.; Henderson, W. A.; Appetecchi, G. B.; Alessandrini, F.; Passerini, S., Recent developments in the ENEA lithium metal battery project. *Electrochim. Acta* **2005**, *50* (19), 3859-3865, <https://doi.org/10.1016/j.electacta.2005.02.049>.
79. Wang, F.; Li, L.; Yang, X.; You, J.; Xu, Y.; Wang, H.; Ma, Y.; Gao, G., Influence of additives in a PVDF-based solid polymer electrolyte on conductivity and Li-ion battery performance. *Sustain. Energy Fuels* **2018**, *2* (2), 492-498, <https://doi.org/10.1039/C7SE00441A>.



[Supplementary Material]

**Y-doped  $\text{LiZr}_2(\text{PO}_4)_3$  in PVDF-HFP Composite Electrolyte for Solid State Li Metal Batteries**

Pratiksha Gami<sup>a</sup>, Manish Badole<sup>a</sup>, Hari Narayanan Vasavan<sup>a</sup>, Asish Kumar Das<sup>a</sup>, Samridhi Saxena<sup>a</sup>, and Sunil Kumar<sup>a,b,\*</sup>

<sup>a</sup>Department of Metallurgical Engineering and Materials Science, Indian Institute of Technology Indore, Simrol, 453552, India.

<sup>b</sup>Center for Electric Vehicle and Intelligent Transport Systems, Indian Institute of Technology Indore, Simrol, 453552, India

\* Corresponding author

Corresponding author E-mail: sunil@iiti.ac.in

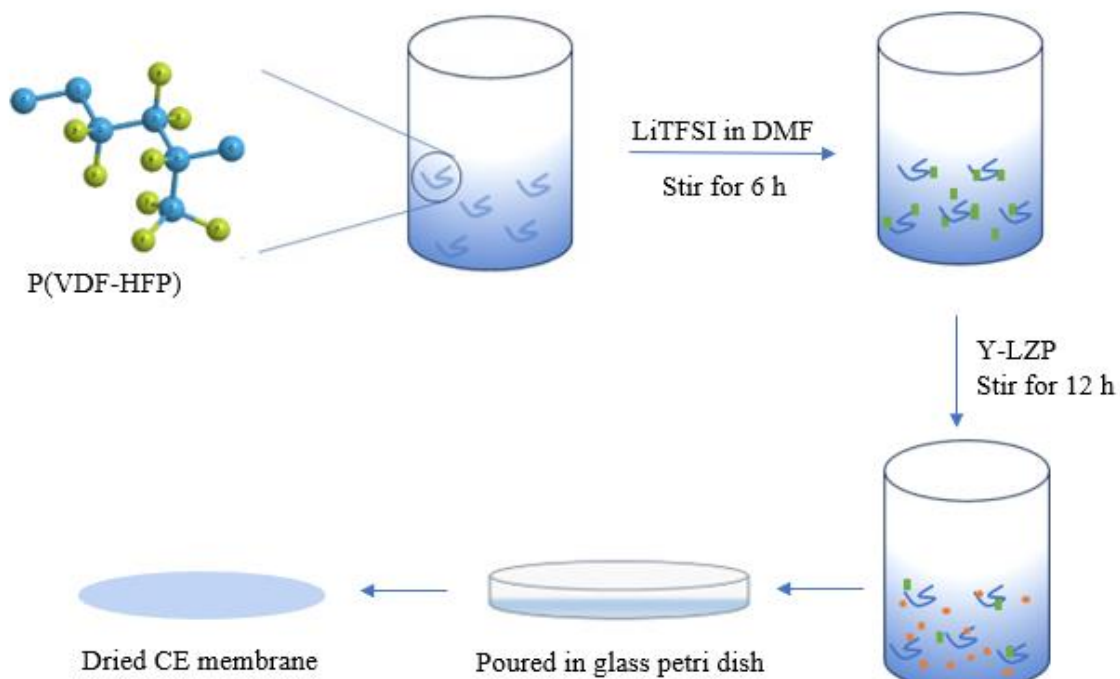


Figure S1: Schematic of preparation of CE membrane film.

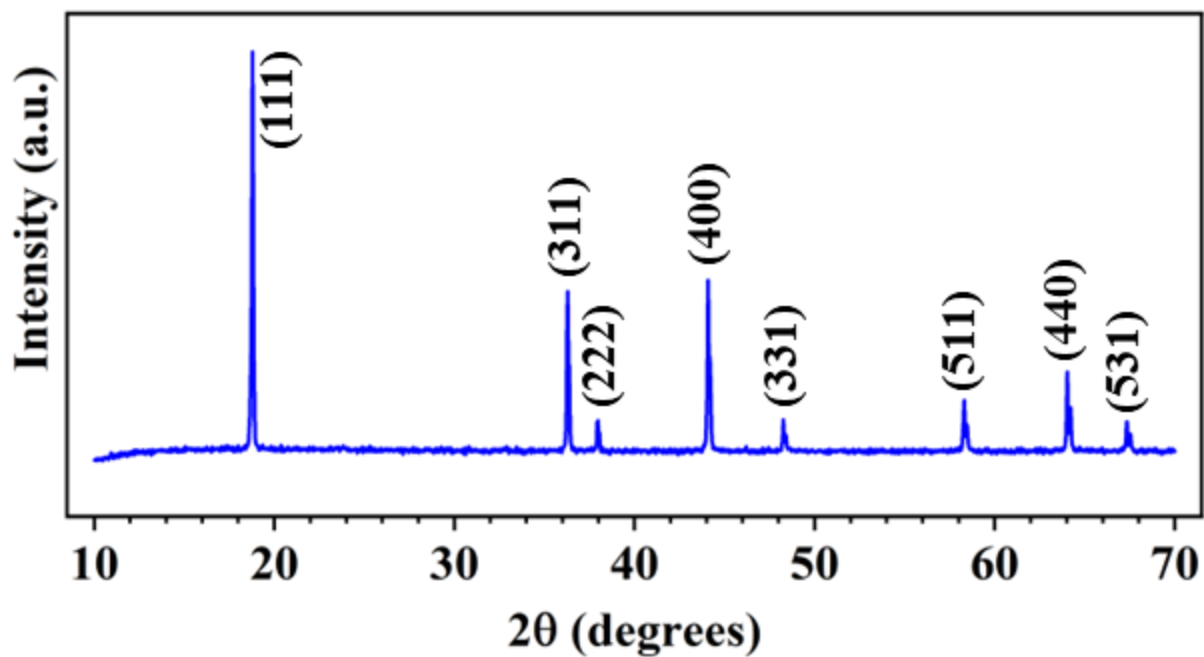


Figure S2: XRD pattern of commercial  $\text{LiMn}_2\text{O}_4$  coated on Aluminum foil.

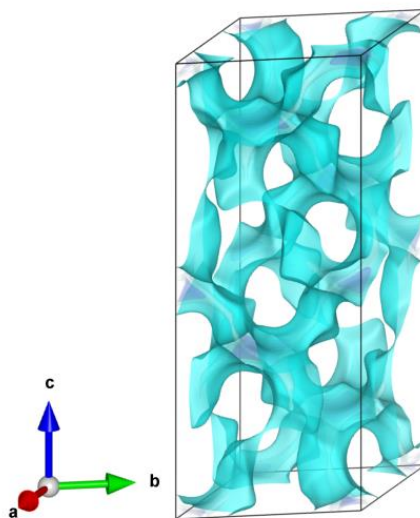


Figure S3: Lithium-ion migration pathways in rhombohedral Y-LZP unit cell.

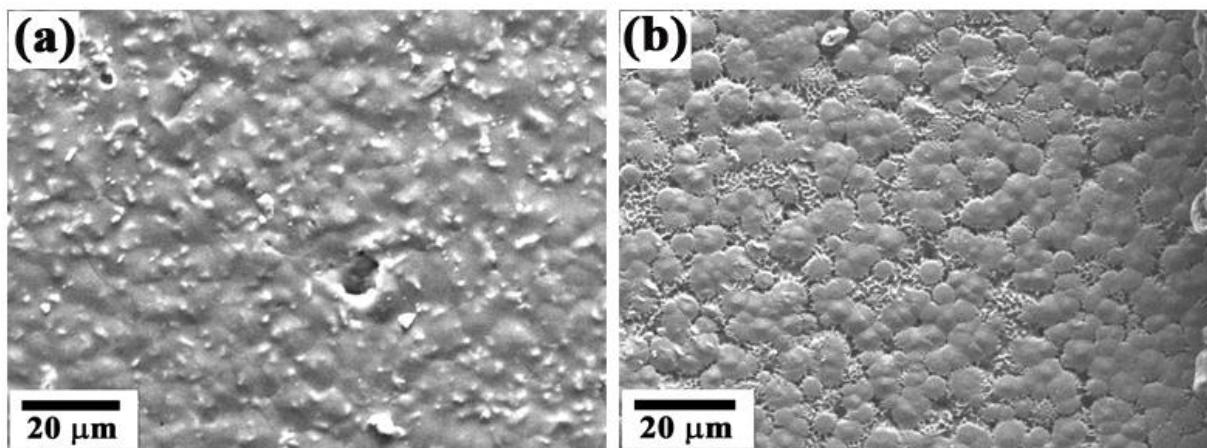


Figure S4: SEM micrographs of (a) CE10 membrane and (b) CE20 membrane.

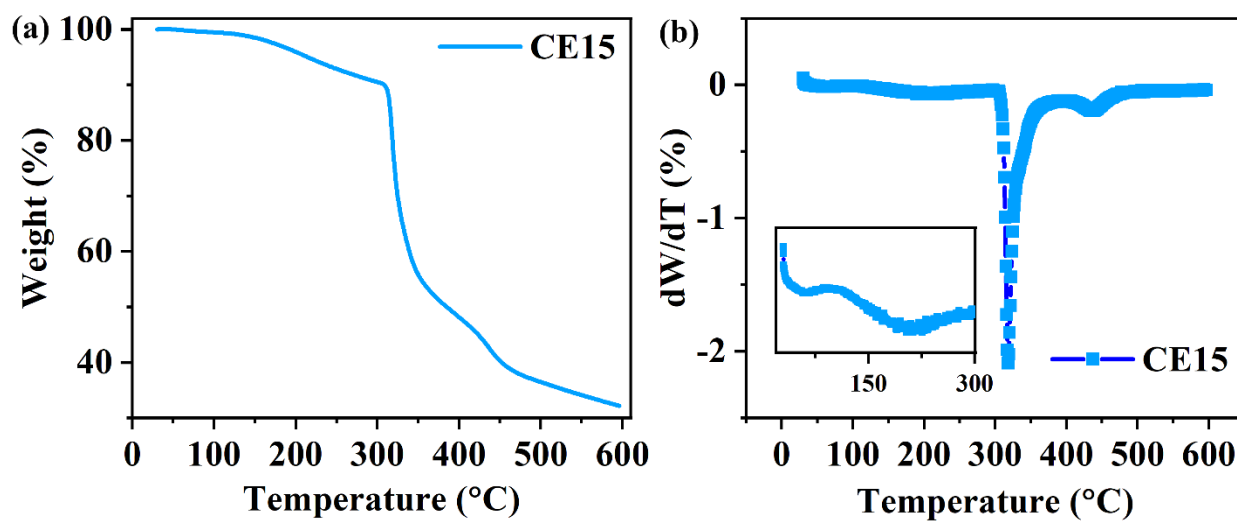


Figure S5: (a) TGA and (b) differential-TGA plots of CE15 membrane.

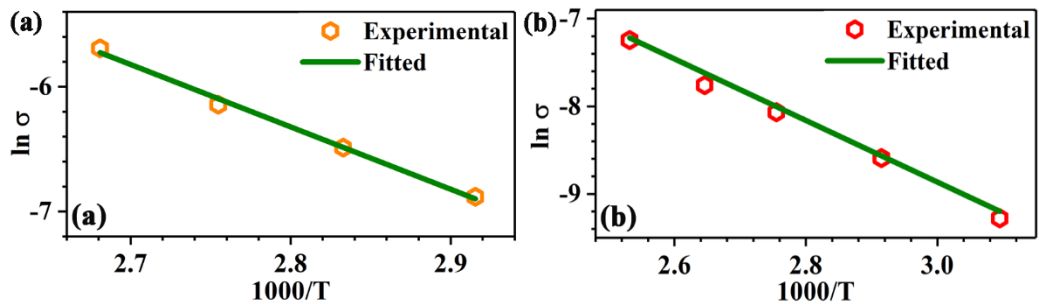


Figure S6. Arrhenius fitting of the temperature dependent conductivity of (a) CE15 membrane and (b) Y-LZP ceramic pellet.

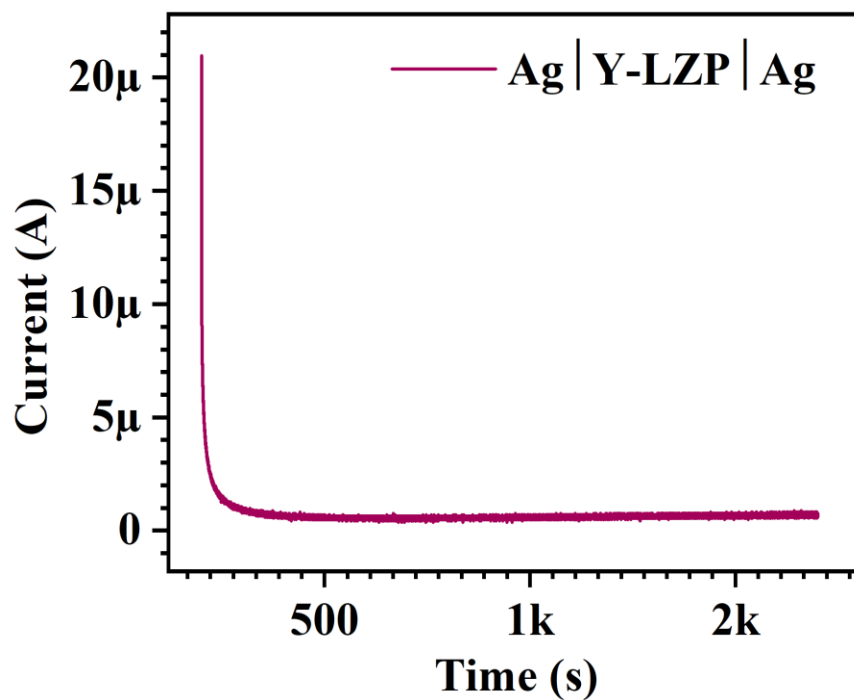


Figure S7: Chronoamperometry profile of Y-LZP.

**Table S1:** Li<sup>+</sup> transference number ( $t_{\text{Li}^+}$ ) calculation for CE0, CE05, CE10, CE15, and CE20 (applied DC voltage = 50 mV).

<b>CE<sub>x</sub></b>	<b><math>t_{\text{Li}^+}</math></b>
CE0	0.24
CE05	0.31
CE10	0.38
CE15	0.64
CE20	0.47